NAVAL POSTGRADUATE SCHOOL

MONTEREY, CALIFORNIA

THESIS

NOVEL OUT-COUPLING TECHNIQUES FOR
TERAHERTZ FREE ELECTRON LASERS

by

Steven E. Grey, Jr.

June 2012

Thesis Co-Advisors:	Keith R. Cohn
	William B. Colson
Second Reader:	Joseph Blau

Approved for public release; distribution is unlimited

THIS PAGE INTENTIONALLY LEFT BLANK

REPORT DOCUMENTATION PAGE		*Form Approved OMB No. 0704-0188*

Public reporting burden for this collection of information is estimated to average 1 hour per response, including the time for reviewing instruction, searching existing data sources, gathering and maintaining the data needed, and completing and reviewing the collection of information. Send comments regarding this burden estimate or any other aspect of this collection of information, including suggestions for reducing this burden, to Washington headquarters Services, Directorate for Information Operations and Reports, 1215 Jefferson Davis Highway, Suite 1204, Arlington, VA 22202-4302, and to the Office of Management and Budget, Paperwork Reduction Project (0704-0188) Washington DC 20503.

1. AGENCY USE ONLY *(Leave blank)*	2. REPORT DATE June 2012	3. REPORT TYPE AND DATES COVERED Master's Thesis	
4. TITLE AND SUBTITLE Novel Out-Coupling Techniques for Terahertz Free Electron Lasers		5. FUNDING NUMBERS	
6. AUTHOR(S) Steven E. Grey, Jr.			

7. PERFORMING ORGANIZATION NAME(S) AND ADDRESS(ES)
    Naval Postgraduate School
    Monterey, CA 93943-5000
		8. PERFORMING ORGANIZATION REPORT NUMBER	

9. SPONSORING /MONITORING AGENCY NAME(S) AND ADDRESS(ES) N/A		10. SPONSORING/MONITORING AGENCY REPORT NUMBER	

11. SUPPLEMENTARY NOTES The views expressed in this thesis are those of the author and do not reflect the official policy or position of the Department of Defense or the U.S. Government. IRB Protocol number _____N/A_____.

12a. DISTRIBUTION / AVAILABILITY STATEMENT Approved for public release; distribution is unlimited	12b. DISTRIBUTION CODE

13. ABSTRACT (maximum 200 words)

There are several issues that are encountered when designing a Free Electron Laser (FEL) oscillator in the terahertz (THz) regime. One such issue is that there are few inexpensive materials that are suitable for forming a semi-transparent out-coupling mirror. In an attempt to mitigate this particular issue, the focus of this presentation is to explore various out-coupling techniques for a notional FEL oscillator in the THz regime. The advantages and disadvantages of several out-coupling methods will be discussed, including hole out-coupling, and double mesh out-coupling. Simulation results will be presented, showing the effects of these various methods on FEL extraction and optical beam quality.

14. SUBJECT TERMS Free Electron Laser, FEL, Terahertz, THz, FEL Simulations , out-coupling, mesh out-coupler, hole out-coupler			15. NUMBER OF PAGES 63
			16. PRICE CODE
17. SECURITY CLASSIFICATION OF REPORT Unclassified	18. SECURITY CLASSIFICATION OF THIS PAGE Unclassified	19. SECURITY CLASSIFICATION OF ABSTRACT Unclassified	20. LIMITATION OF ABSTRACT UU

NSN 7540-01-280-5500

Standard Form 298 (Rev. 2-89)
Prescribed by ANSI Std. 239-18

THIS PAGE INTENTIONALLY LEFT BLANK

NOVEL OUT-COUPLING TECHNIQUES FOR TERAHERTZ FREE ELECTRON LASERS

Steven E. Grey, Jr.
Lieutenant, United States Navy
B.S., United States Naval Academy, 2006

Submitted in partial fulfillment of the
requirements for the degree of

MASTER OF SCIENCE IN APPLIED PHYSICS

from the

**NAVAL POSTGRADUATE SCHOOL
June 2012**

Author: Steven E. Grey, Jr.

Approved by: Keith R. Cohn
                 Thesis Co-Advisor

                 William B. Colson
                 Thesis Co-Advisor

                 Joseph Blau
                 Second Reader

                 Andrès Larraza
                 Chair, Department of Physics

THIS PAGE INTENTIONALLY LEFT BLANK

ABSTRACT

There are several issues that are encountered when designing a Free Electron Laser (FEL) oscillator in the terahertz (THz) regime. One such issue is that there are few inexpensive materials that are suitable for forming a semi-transparent out-coupling mirror. In an attempt to mitigate this particular issue, the focus of this thesis is to explore various out-coupling techniques for a notional FEL oscillator in the THz regime. The advantages and disadvantages of several out-coupling methods will be discussed, including hole out-coupling, and double mesh out-coupling. Simulation results will be presented, showing the effects of these various methods on FEL extraction and optical beam quality.

THIS PAGE INTENTIONALLY LEFT BLANK

TABLE OF CONTENTS

LIST OF FIGURES

LIST OF TABLES

THIS PAGE INTENTIONALLY LEFT BLANK

LIST OF ACRONYMS AND ABBREVIATIONS

3D	Three-Dimensional
CGS units	centimeter, grams, seconds
CVD	Chemical Vapor Deposition Diamond,
ERL	Energy Recovery LINAC
FPI	Fabry-Perot Interferometer
FEL	Free Electron Laser
GeV	Giga-electron volts
HRFZ Si	High resisitivity Float Zone Sillicon
MeV	Mega-electron volts
mm	millimeter
NPS	Naval Postgraduate School
pC	pico-coulomb
RF LINAC	radio frequency linear accelerators
RMS	root mean squared
THz	Terahertz

THIS PAGE INTENTIONALLY LEFT BLANK

I.   INTRODUCTION

A Free Electron Laser (FEL) that uses electrons that are not bound to an atom to create coherent light. This type of laser has many attributes that distinguish it from the myriad of different lasers used worldwide. One characteristic is that FELs are tunable over a wide range of the electromagnetic spectrum and can be designed to create virtually any wavelength of light, from microwave to X-ray. This is because FELs do not depend on a conventional gain medium to produce the coherent photons; rather, the photons produced are a result of the electron interaction with a magnetic and optical field. The FEL can be operated at much higher energies than other conventional lasers since there is no gain medium to be damaged.

This thesis will be exploring a notional FEL operating in the Terahertz (THz) regime of the electromagnetic spectrum. Operating in this regime does present some unique issues. The first issue presented is that of clipping, which will be explained in a later chapter. Briefly, clipping is an issue because of long wavelength associated with THz. Another issue is that many materials are not transparent to THz light. This makes it more difficult to extract usable light created in the FEL cavity. This issue is the motivation behind the study of various out-coupling techniques for an FEL.

The methods of out-coupling to be explored will consist of hole out-coupling and mesh out-coupling. Hole out-coupling utilizes a highly reflective material with a hole in the center as the out-coupling mirror and mesh out-coupling uses a fine metallic mesh grid structure in place of the mirror.

The notional FEL will be in the oscillator configuration. The components of this configuration will be described later in this chapter.

A.   FEL COMPONENTS

A FEL in the oscillator configuration is comprised of several components. The major components as shown in Figure 1 include the injector, the accelerator, the undulator, the optical cavity, the energy recovery area, and the beam dump.
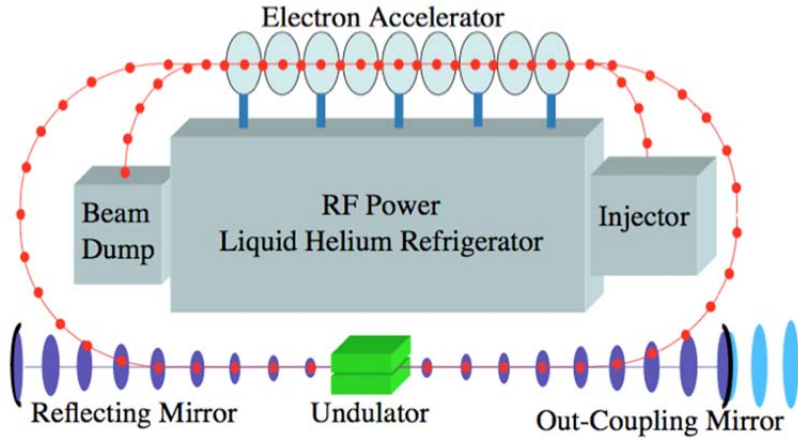
Figure 1. FEL in the oscillator configuration. Red dots are electrons, purple ellipses are light, and light blue ellipses are out coupled light. From [1]

1. Injector

The injector is where the "free" electrons are created from the cathode. The processes by which electrons are emitted from the cathode surface include thermionic emission and the photoelectric effect. Thermionic emission utilizes a heated cathode that emits electrons from its surface. The photoelectric effect uses light pulses that are incident on the photocathode. If the energy of the light is greater than the work function of the cathode, then electron pulses will be emitted [2]. The emitted electron pulses are then accelerated using a static or oscillating electric field to around 5 MeV.

2. Accelerator

The electron pulse next enters the accelerator. Many accelerators are superconducting radio frequency linear accelerators (RF LINAC) that have niobium cavities that require liquid helium for cooling. In this stage, an electron pulse travels through each cavity in phase with the oscillating RF field inside the cavity. As a result, the electrons can be accelerated to a highly relativistic energy, 100 MeV for typical applications. The FEL can have electrons that have energies ranging from 5 MeV to 15 GeV.

3. Undulator

The undulator is composed of a series of permanent magnets that are arranged in alternating polarity and are often spaced equally. As the electrons pass through, the Lorentz Force causes them to "wiggle" as they travel. As the electrons wiggle, they create a light pulse that has a wavelength much shorter than the undulator period because of relativistic Doppler shifts. Only a small percentage of the energy of the electron pulse is converted into light.

4. Optical Cavity

The optical cavity is the region of the FEL where coherent light is amplified. The components of this region are only used in the oscillator configuration. The oscillator configuration uses a short undulator and two mirrors. One of the mirrors is highly reflective and reflects the created light pulse back through the undulator for stimulated emission and coherence evolution. The out-coupling mirror is typically partially transparent and allows for a small percentage of the light to pass through.

5. Energy Recovery (The Beam Dump)

Since only a small percentage of the energy of the electrons is converted to light, some FELs direct the electrons to pass through the RF accelerator again with the RF field ~180-degrees out of phase. This causes the electrons to lose energy to the RF field, and prevents high energy electrons from entering the electron beam dump. This reduces the amount of shielding needed for any applications. This type of configuration is call an Energy Recovery LINAC (ERL), since it recovers most of the unused energy in the electron pulse, thus improving the overall efficiency.

B.   FEL THEORY

1.   FEL "Pendulum" Equation and Electron Dynamics

The dynamics of electron motion as it passes through the undulator are governed by the following equations:

$$\frac{d(\gamma \vec{\beta})}{dt} = -\frac{e}{mc}\left(\vec{E} + \vec{\beta} \times \vec{B}\right),$$ (I.1)

$$\frac{d\gamma}{dt} = -\frac{e}{mc}\vec{\beta} \cdot \vec{E},$$ (I.2)

$$\gamma = \frac{1}{\sqrt{1-\vec{\beta}^2}},$$ (I.3)

where $\vec{E}$ and $\vec{B}$ are the electric and magnetic fields, respectively, $e = |e|$ is the charge magnitude of an electron, m is the mass of an electron, $\vec{\beta} = \vec{v}/c$ is the dimensionless electron velocity, and γ is the relativistic Lorentz factor [1]. Equation I.1 is the Lorentz force equation and governs the motion of the electron as it encounters FEL fields. Equation I.2 is the rate of energy change due to the work done by the electric field. This equation calculates the energy given to the optical field by the electron.

As the electrons travel through the undulator, they interact with the electric and magnetic fields of the light, $\vec{E} = E\left(\cos\psi, -\sin\psi, 0\right)$, $\vec{B} = E\left(\sin\psi, \cos\psi, 0\right)$ where E is the field amplitude in cgs units, $\psi = kz - \omega t + \phi$, with ϕ the optical phase, $k = 2\pi/\lambda$ the wave number, λ the wavelength, and ω the optical frequency. The electrons also interact with the magnetic field of the undulator, $\vec{B} = B\left(\cos(k_0 z), \sin(k_0 z), 0\right)$, where B is the undulator field strength, and $\lambda_0 = 2\pi/k_0$ is the undulator period [1]. The electrons at this point are highly relativistic, so $\beta_z \approx 1$, so when the fields are substituted into Equation I.1, the transverse motion in the undulator is approximately determined only by,

$$\overrightarrow{\beta_\perp} \approx -\frac{K}{\gamma}\left(\cos(k_0 z), \sin(k_0 z), 0\right)$$

(I.4)

where $K = eB_{rms}\lambda_0/(2\pi mc^2)$ is the dimensionless undulator parameter, and B_{rms} is the rms value of the undulator field. Typically $K \approx 1$ for most FELs [3]. If Equation I.4 is substituted into Equation I.2, the electron's energy evolution yields

$$\dot{\gamma} = \frac{d\gamma}{dt} = -\frac{e}{mc}E\left[\beta_x \cos\psi - \beta_y \sin\psi\right] = \frac{eKE}{\gamma mc}\cos(\zeta + \phi)$$

(I.5)

where $\zeta = (k + k_0)z - \omega t$ is the "electron phase." The electron phase follows the microscopic position of the electron as it evolves. It is important to note that the energy exchange between the electron and the optical field increases when $\cos(\zeta + \phi) > 0$ and decreases when $\cos(\zeta + \phi) < 0$.

The "electron phase velocity" is defined as $v = \frac{L}{c}\dot{\zeta} = L\left[(k + k_0)\beta_z - k\right] = \overset{\circ}{\zeta}$,

where $(\overset{\circ}{...})$ indicates a derivative with respect to dimensionless time $\tau = ct/L$ with L the length of the undulator so that τ varies from 0 to 1 [1]. If $v = 0$, the energy exchange is at an optimum level and the FEL is said to be at "resonance." In this condition, the electron phase velocity is manipulated to show that the resonant laser wavelength is

$$\lambda = \frac{\lambda_0(1 - \beta_z)}{\beta_z} \approx \frac{\lambda_0(1 - K^2)}{2\gamma_0^2}$$

(I.6)

where γ_0 is the initial electron beam Lorentz factor and $\gamma_0 \gg 1$.

In a beam of electrons, each electron will have a unique initial phase $\zeta(0) = \zeta_0 = (k + k_0)z_0$ as they enter the undulator. In a typical FEL, $\sim 10^6$ electrons are randomly spread in each section of the electron beam $\sim \lambda$ in length. This means that roughly half of the electrons will lose energy to the laser field and half will take energy, as described in Equation I.5. A change in the electrons energy will also create a change in the position, ζ and the electron phase velocity, v. The change in the phase velocity is

5

$\dot{v} = 4\pi\dot{\gamma}/\gamma_0$ while near resonance in the relativistic limit [1]. If this is combined with Equation I.5, then the FEL "pendulum equation" is derived

$$\dot{v} = \ddot{\zeta} = |a|\cos(\zeta + \phi),$$

(I.7)

where $|a| = 4\pi NeKLE/\gamma_0^2 mc^2$ is the dimensionless laser field amplitude[1]. From this, it is shown that changes in the design of the FEL will affect the dimensionless amplitude of the laser field. If the electron beam has a larger Lorenz factor, the strength of the laser field will need to increase in order to create the same dimensionless amplitude.

2. FEL Wave Equation

Having solved for the microscopic motion of the electrons in the undulator, the evolution of the laser field in the undulator must be derived. Consider the full vector wave equation with the Coloumb gauge [3]

$$\left(\nabla^2 - \frac{1}{c^2}\frac{\partial^2}{\partial t^2}\right)\vec{A}(\vec{x},t) = \frac{4\pi}{c}\vec{J}_\perp(\vec{x},t),$$

(I.8)

where $\vec{J}_\perp = -e\sum_i \vec{\beta}_\perp \delta^{(3)}\left(\vec{x} - \vec{r}_i(t)\right)$ is the transverse current density, $\vec{r}_i(t)$ is the electron position at time t, and $\vec{A}(\vec{x},t)$ is the optical vector potential. The electric and magnetic fields of the laser can be derived using the vector potential,

$$\vec{E} = \frac{1}{c}\frac{\partial\vec{A}}{\partial t}, \quad \vec{B} = \vec{\nabla}\times\vec{A}.$$

(I.9)

For the case of laser light, the beam is partially or completely coherent and $\vec{A}(\vec{x},t)$ has a slowly-varying envelope $E(\vec{x},t)$ in the direction of propagation along the z axis [3]. If the electric field is assumed to be complex and slow-varying over an optical wavelength, the optical vector potential is assumed to have the form

$$\vec{A}(\vec{x},t) = \frac{E(\vec{x},t)}{k}\hat{\varepsilon}e^{i(kz - \omega t)},$$

(I.10)

6

where $E = |E|e^{i\phi}$ is the complex laser electric field, and $\hat{\varepsilon}$ is the polarization vector of the laser field. If the electric field amplitude $|E(\vec{x},t)|$ and the phase $\phi(\vec{x},t)$ are assumed to be slow-varying along the z axis [3], Equation I.8 can be rewritten as

$$\frac{\hat{\varepsilon}e^{i(kz-\omega t)}}{k}\left[\vec{\nabla}_{\perp}^2 + 2ik\left(\frac{\partial}{\partial z} + \frac{1}{c}\frac{\partial}{\partial t}\right)\right]E \approx -\frac{4\pi}{c}\vec{J}_{\perp}$$ (I.11)

Both sides of the equation are multiplied by $ke^{-i(kz-\omega t)}\hat{\varepsilon}^*$ and a new coordinate, $u = z - ct$, is introduced in order to invoke the method of characteristics[1]. With that, Equation I.11 becomes the paraxial wave equation with a source current

$$\left[\vec{\nabla}_{\perp}^2 + 2ik\left(\frac{1}{c}\frac{\partial}{\partial t}\right)\right]E = -\frac{4\pi k}{c}\vec{J}_{\perp}\cdot\hat{\varepsilon}^*e^{-i(kz-\omega t)}$$ (I.12)

Using the relationship between the transverse motion of an electron and the transverse current density defined previously, Equation I.12 becomes

$$\left[\vec{\nabla}_{\perp}^2 + \frac{2ik}{c}\frac{\partial}{\partial t}\right]E = -4\pi ieKk\rho(\vec{x},t)<e^{-i\zeta}/\gamma>_{(\vec{x},t)}$$ (I.13)

where $\rho(\vec{x},t)$ is the local electron density in a small volume element dV located at $(\vec{x},t)$, and $<...>$ represents an average over sample electrons in that volume element.

Dimensionless time, τ, is reintroduced and the wave equation is multiplied by the factor $-4\pi NeKL^2/\gamma_0^2 mc^2 k$ so that it becomes

$$\left[-\frac{iL}{2k}\vec{\nabla}_{\perp}^2 + \frac{\partial}{\partial\tau}\right]a(\vec{x},\tau) = -<je^{-i\zeta}>_{(\vec{x},\tau)}$$ (I.14)

where $a = |a|e^{i\phi}$ is the complex laser field, $|a| = 4\pi NeKLE/\gamma_0^2 mc^2$ is again the dimensionless laser field amplitude, $j = 8\pi^2 Ne^2 K^2 L^2 \rho/\gamma_0^3 mc^2$ is the "dimensionless FEL density," and it is assumed that $\gamma \approx \gamma_0$ for all the electrons in the beam[3].

7

The wave equation is made completely dimensionless by defining the dimensionless transverse coordinates $\tilde{x} = x(k/2L)^{1/2}$, and $\tilde{y} = y(k/2L)^{1/2}$. The wave equation is now written as

$$\left[-\frac{i}{4}\vec{\nabla}_{\perp}^2 + \frac{\partial}{\partial\tau} \right] a(\vec{x}, \tau) = - < je^{-i\zeta} >_{(\vec{x},\tau)} ,$$

(I.15)

where the coordinates (x, y, z, τ) are now all dimensionless. When the laser beam and the electron beam overlap and diffraction is small over the undulator length, the FEL wave equation can be written in its simplest form

$$\overset{\circ}{a} = -j < e^{-i\zeta} > .$$

(I.16)

8

II.   THZ ISSUES

A.   MATERIAL CONSIDERATIONS

For the purpose of this thesis THz radiation is defined to be in the range of 100 microns to 1mm. There are several issues that arise when out-coupling THz radiation in a FEL oscillator in this range. Typically, FELs use a partially transparent mirror to out-couple the light from inside the optical cavity. These mirrors consist of a substrate that is then layered with a coating that is reflective to the wavelength of light being used. As such, there are several material properties of the mirror substrate that must be accounted for in order to produce usable THz light for the FEL.

1.   Transmission of Radiation

In order for a FEL to operate, a fraction of the light produced in the optical cavity must be transmitted through the out-coupling mirror of the resonator. THz radiation is absorbed by many materials, which often leads to the need for expensive materials to be used.

The fraction of incident radiation absorbed can be calculated by:

$$A = 1 - \left(1 - R\right)e^{-\alpha x}$$

where A is the fraction of radiation absorbed, R is the reflection coefficient, α is the absorption coefficient, and x is the thickness of the material [4]. This shows that with an increase of the thickness of the material or with an increase in the absorption coefficient, the fraction of light absorbed increases. This absorbed energy manifest itself as heat and can result in other effects on the mirror.

2.   Thermal Expansion

When a majority of materials are heated by a source, there is a tendency for the materials to expand. This thermal expansion is found experimentally and calculated by:

$$\alpha_T = \frac{1}{L}\left(\frac{\partial L}{\partial T}\right)$$

$$\beta = \frac{1}{V}\left(\frac{\partial V}{\partial T}\right);$$

where α_T and β are the coefficients of linear and volumetric expansion, respectively, L and V are the materials length and volume, respectively, and T is temperature [5]. From these two equations, it can be seen that in order to have a material that exhibits minimal change in dimension, the material in question must have a small coefficient of expansion. A minimal change in dimension is critical in order to prevent optical distortions, which can lead to the laser either not operating at the optimal levels or not operating at all.

3.   Thermal Conductivity

Thermal conductivity describes the ability of materials to conduct and transfer heat. Thermal conductivity is found experimentally and calculated by

$$k = \frac{L}{A(\Delta T)}\left(\frac{dQ}{dt}\right)$$

where k is the thermal conductivity in watts per meter-Kelvin, L is the lateral distance between the temperature difference ΔT, and $\frac{dQ}{dt}$ is the rate of heat flow into the material.[6] The thermal conductivity is shown to be proportional to the heat flow. As such, a material with a large k value will be able to remove heat better than one with small values.

Because the out-coupling mirror absorbs large amounts of energy from the FEL, it is important that the material that comprises the lens be able to transfer the heat from the focal point of the beam. If this is not achieved the beam will distort and/or potentially destroy the mirror.

4.   Insufficiencies

There have been some studies and experiments conducted to identify the optimal material for use with THz radiation. Table 1 provides a summary of selected materials with experimental data for the previously discussed properties. The color scheme of the table is used to highlight material property values in a range that would be suitable for

10

use in a FEL operating in the THz range. As shown, only one of the five materials, Chemical Vapor Deposition (CVD) Diamond, appears to be suitable for use as a mirror. However, even CVD Diamond has its drawbacks. Because CVD Diamond is very expensive, this would lead to a very expensive mirror regardless of the dimension.

Materials	Thermal Conductivity @20 °C (W/M °C)	Thermal Expansion Coefficient (x10-6 / °C)	Transmission Range (µm)
HRFZ Si	1.5	2.6	50 – 300
Quartz	1.3	0.59	< 3
Sapphire	42	5	< 6
Zinc Selenide	18	7.57	10 – 20
CVD Diamond	3300	1.2	10 - 300

Table 1.   Summary of selected materials and respective properties. From [7]

B.   CLIPPING

FEL Beam Clipping is the process by which an optical beam is negated when it comes in contact with an absorbing material. Because of this interaction, a portion of the beam's energy is lost which results in a decrease in power. This phenomenon is most prevalent in the undulator section of the FEL because the beam line is constricted. Figure 2 illustrates how a clipping interaction in the undulator would occur.
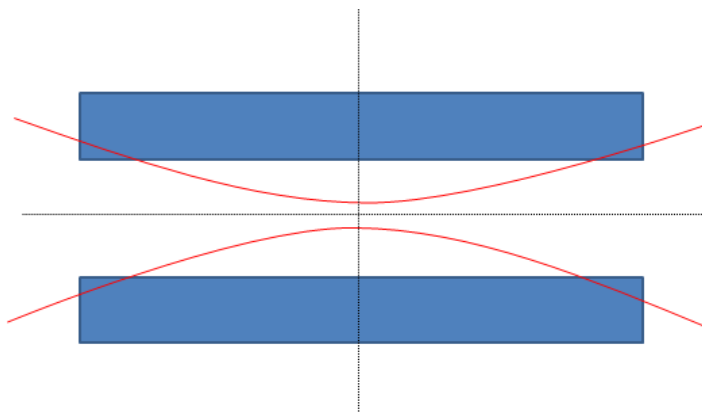

Figure 2.   Clipping in the undulator as a function of diffraction.

A contributor to the degree of severity of the clipping that occurs is beam diffraction. Beam diffraction can be described by

$$w(z) = w_0 \sqrt{1 + z^2 / z_R^2} \, ,$$
(II.1)

where $w(z)$ is the radius of the beam at distance z, w_0 is the optical mode radius and z_R is the Rayleigh length [1]. From Equation II.1, as the distance from $z=0$ increases the radius of the beam also increases. This effect is further exaggerated because the Rayleigh length, defined by

$$z_R = \frac{\pi n w_0^2}{\lambda} \, ,$$
(II.2)

where λ is the optical wavelength, and n ~1 is the index of refraction decreases. As the wavelength increases the Rayleigh length increases which in turn increases the beam radius at distance z. This causes the beam to expand rapidly and as such increases the amount of the beam that potentially will be clipped.

The potential for beam clipping is very prevalent with THz radiation and must be taken into account in accordance with previous studies [7].As such; the simulations that will be conduct will use a constant clipping factor of 4% per pass through the undulator. A separate study of how clipping affects the extraction of energy of the FEL operating in the THz regime will also be conducted in a later chapter.

III. GAUSSIAN MODES

A. GAUSSIAN BEAMS

There are several ways to model the light wave produced by an FEL oscillator. The most convenient approach is to use Gaussian modes. A Gaussian beam in the fundamental transverse mode describes a light wave where the power and intensity of the light are at a maximum at the center of the beam and decrease as the distance from the center increases. This approximation is a solution to the paraxial wave equation.

1. Short Derivation of Paraxial Wave Equation

Consider the wave equation found by solving Maxwell's equations in free space:

$$\nabla^2 \vec{E} = \mu_0 \varepsilon_0 \frac{\partial^2 \vec{E}}{\partial t^2}; \tag{III.1}$$

where the spatial derivatives are taken to be in rectangular coordinates. If it is assumed that $\vec{E}$ is polarized in one direction, so that the scalar form of the wave equation can be invoked

$$\nabla^2 E - \frac{1}{c^2} \frac{\partial^2 E}{\partial t^2} = 0; \tag{III.2}$$

where $1/c^2 = \mu_0 \varepsilon_0$. It can be seen that E has a spatial and temporal dependence. As such, the electric field can be defined as the product of both spatial and temporal factor so that

$$E(x,y,z,t) = E(\vec{r},t) = \widetilde{E}(\vec{r})e^{-i\omega t}; \tag{III.3}$$

where $\omega = (2\pi c)/\lambda = kc$. When substituted into III.2, the wave equation becomes

$$\left(\nabla^2 + k^2\right)\widetilde{E} = 0; \tag{III.4}$$

where $k^2 = \omega^2/c^2$, and the explicit time dependence has been removed from the wave equation [8].

To arrive at the paraxial wave equation from Equation III.4, it is assumed that the transverse beam profile changes slowly on the scale of an optical wavelength. As such, we assume the form

$$\widetilde{E}(x,y,z) = \tilde{u}(x,y,z)e^{-ikz};$$ (III.5)

where $\tilde{u}$ describes the transverse profile of the traveling beam [8]. In other words, $\tilde{u}$ changes slowly in z relative to the factor, e^{-ikz}. When Equation III.5 is substituted into III.4 the wave equation becomes

$$\frac{\partial^2}{\partial x^2}\tilde{u} + \frac{\partial^2}{\partial y^2}\tilde{u} + \frac{\partial^2}{\partial z^2}\tilde{u} - 2ik\frac{\partial}{\partial z}\tilde{u} = 0.$$ (III.6)

In III.6 the second derivative of the z component of $\tilde{u}$ can be assumed to be negligible by invoking the paraxial approximation, $\left|\partial^2\tilde{u}/\partial z^2\right| \ll \left|2k\,\partial\tilde{u}/\partial z\right|$ [8]. From this, Equation III.6 can be rewritten as the paraxial wave equation:

$$\left(\nabla_\perp^2 - 2ik\frac{\partial}{\partial z}\right)\tilde{u} = 0;$$ (III.7)

where $\nabla_\perp^2 = \partial^2/\partial x^2 + \partial^2/\partial y^2$. This approximation remains valid for traveling beams that propagate at an angle less than 30 degrees with the z-axis. Due to this, the paraxial approximation holds true for most FELs in the oscillator configuration.

B. HERMITE-GAUSSIAN BEAMS

A solution to the paraxial wave equation must be found in order to properly model a propagating beam. One such solution is the Hermite-Gaussian solution,

$$E_{l,m}(x,y,z) = E_0 \frac{w_0}{w(z)} H_l\left(\sqrt{2}\frac{x}{w(z)}\right) H_m\left(\sqrt{2}\frac{y}{w(z)}\right)$$
$$\times \exp\left[-ik\frac{x^2+y^2}{2R(z)} - \frac{x^2+y^2}{w^2(z)} - ikz + i(l+m+1)\eta(z)\right].$$ (III.8)

This solution is very intricate yet it is still in the form of $\widetilde{E}(x,y,z) = \widetilde{u}(x,y,z)e^{-ikz}$ [8]. The waist size term, $w(z)$, was initially defined by Equation II.1. $R(z)$ is the radius of curvature of the propagating beam and it is given by $R(z) = z\left(1 + \left(z_R^2/z^2\right)\right)$. From this definition, it can be seen that the radius of curvature changes depending on whether the beam is propagating in the positive or negative direction. $\eta(z)$ represents a phase shift defined by $\eta(z) = \arctan\left(z/z_R\right)$. The l and m labels are integer indices of the Hermite polynomials, H_l and H_m. These indices ultimately affect the transverse intensity of the beam and are referred to as modes. The $l=0$, $m=0$ mode is called the "fundamental" mode because the subsequent Hermite polynomials are both more structured. Figure 3 displays several of the lower order spatial modes that the beam can assume.
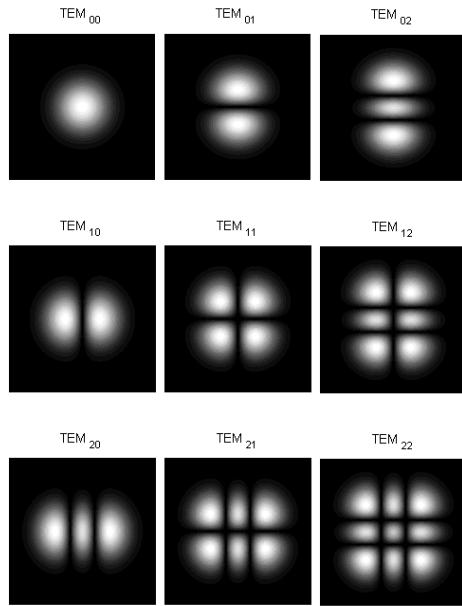

Figure 3.   Transverse Electromagnetic Modes. From [9]

For the purpose of the FEL, the fundamental mode is often preferred because the beam can be later focused into a tighter spot for a given set of focusing elements. For the purposes of directed energy, this means more power can be delivered to a smaller spot on a distant target.

THIS PAGE INTENTIONALLY LEFT BLANK

IV.   HOLE OUT-COUPLING

With hole out-coupling, the light created in the FEL optical cavity is transmitted through a hole in a highly-reflecting mirror instead of being transmitted through a partially transparent mirror. This technique has been shown to work for other types of lasers operating at various wavelengths [10].

A.   DESIGN PARAMETERS

For the hole out-coupling simulations, Table 2 lists the design parameters that were held constant:

$E_b \sim 5$ MeV	$f \sim 50$ MHz	$N = 16$
$\lambda_0 \sim 2$ cm	$\lambda \sim 100$ μm	$K \sim 0.35$

Table 2.   FEL Parameters

where E_b is the beam kinetic energy, f is the pulse repetition frequency, N is the number of undulator periods, λ_0 is the undulator period, λ is the optical wavelength, and K is the dimensionless undulator parameter.[3]

B.   SIMULATION RESULTS

Simulations were conducted using the NPS 3D oscillator FEL code and were categorized into two groups based on the electron bunch charge, 100pC and the 200pC.

1.   100pC Bunch Charge Simulations

Simulations were conducted for the 100pC bunch charge varying the radius of the hole, the quality factor *Q*, and the clipping gap.

a.   *Varying Hole Radius with a high Q value*

In the first set of simulations conducted for the 100pC bunch charge, the hole radius was varied over a range of values. The quality factor, *Q*, is defined to be inversely proportional to the amount of loss in a cavity without a hole. For this set of

simulations, Q was set at a very large value ($\sim 10^{10}$) in order to approximate a highly-reflecting mirror surface. This means that essentially no light is absorbed by the mirrors, thus the only way for the light to escape is through the hole. The hole radius range was from 0.05 cm to 0.40 cm. The simulation results are plotted in Figure 4. The shape of the plot shows that there is a peak of ~2.8% extraction at a hole radius of 0.125 cm. This is due to how the electrons are evolving to produce the light, as will be seen in subsequent figures.

**Extraction for a Highly Reflective Surface with a Hole**
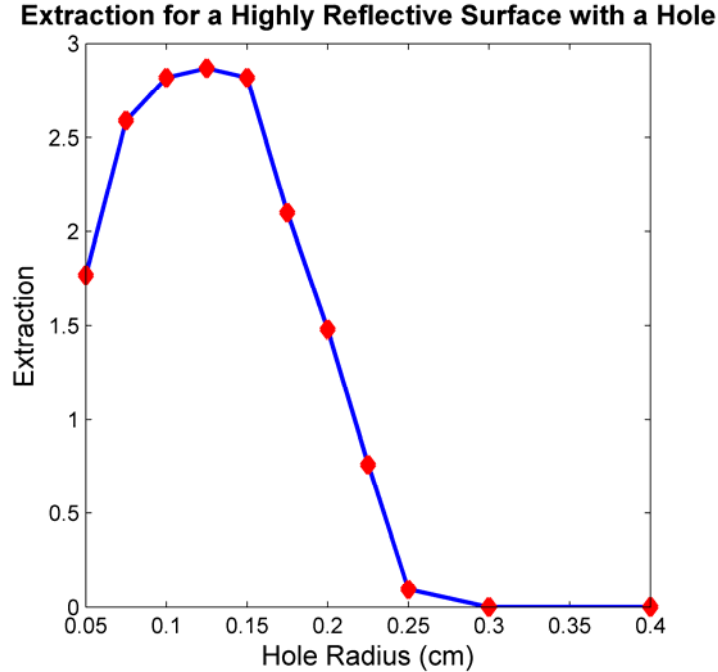
Figure 4.   Simulations results for 100pC bunch charge with $Q=10^{10}$

Figure 5 (a) displays the optical field evolution in the undulator for the hole radius of 0.05 cm. The blue/cyan area represents the optical field, the red dots are the electrons, and the yellow curves represent the mode of the beam at the ends of the undulator.   In this case the peak dimensionless optical amplitude is high, $|a| \approx 52$. indicating FEL saturation in strong optical fields..   With a small hole only a small fraction of the light produced in the optical cavity is out-coupled. The optical field grows to saturation, while the electrons also evolve described by the "pendulum" equation and

18

the FEL wave equation. In Figure 5 (b), the electrons appear to overbunch as they travel farther in their phase space orbits, absorbing energy from the optical field and hence reducing the extraction.
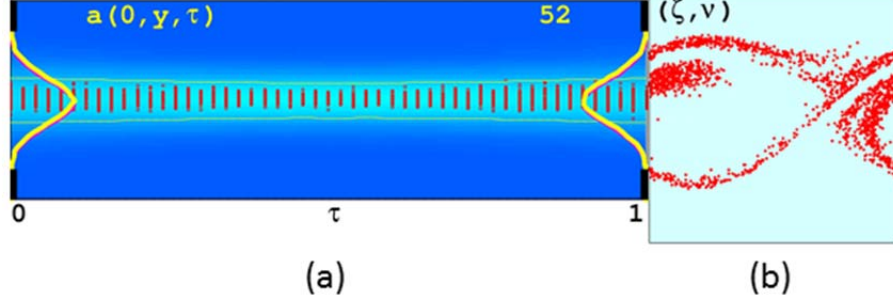

Figure 5.   Simulation output for hole radius of 0.05 cm. (a) The optical field evolution in the undulator. (b) The electron evolution phase space plot at the end of the undulator.

The optimal hole radius of 0.125 cm gives the largest amount of optical power out of the FEL mirror hole. The peak optical field is smaller ($|a| = 27$) than that of the smaller hole radius, since a greater fraction of the light is out-coupled per pass. Figure 6 (b) shows the electrons do not overbunch as severely, and hence more energy is converted to light and out-coupled through the mirror.
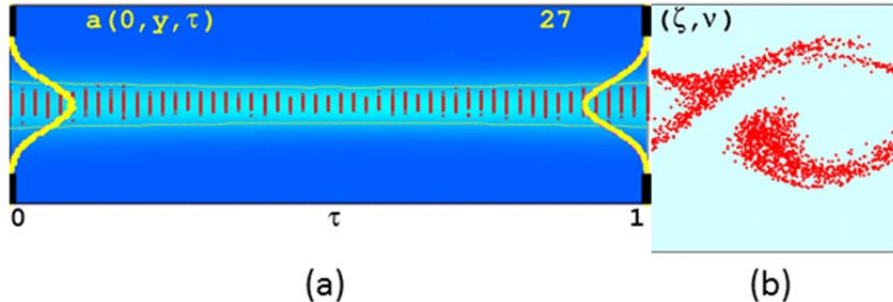

Figure 6.   Simulation output for hole radius of 0.125 cm.

If the hole radius becomes too large, too much of the light escapes from the cavity which causes a drop in the dimensionless field amplitude ($|a| = 2.4$) as seen in

Figure 7 (a). Due to this, the electrons do not evolve much in phase space, as seen in Figure 7 (b), and very little energy is extracted from them.
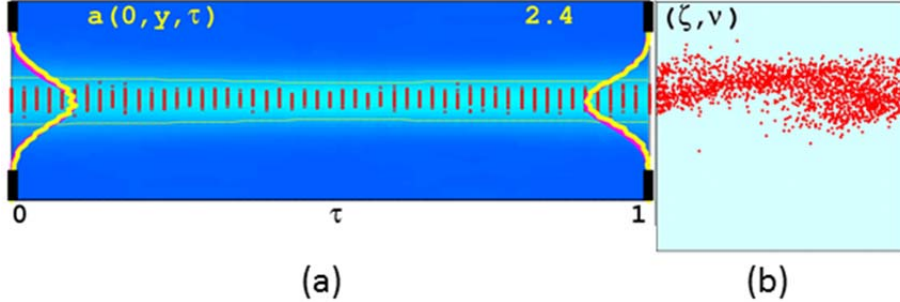

Figure 7.　Simulation output for hole radius of 0.25 cm.

The use of hole out-coupling did have a negative effect on the transverse mode shape. As seen in Figure 8, as the size of the hole increased, small perturbations in the mode shape at the out-coupling mirror started to develop. The beam is losing energy to the formation of higher-order modes, which is not a favorable condition for the FEL interaction and applications.
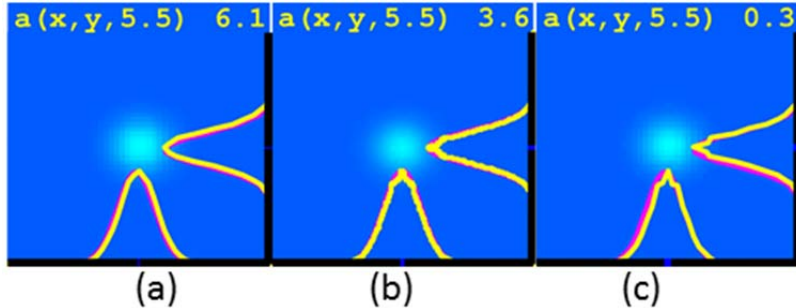
Figure 8.　Transverse mode shape at the out-coupling mirror for a hole radius of:(a) 0.05 cm, (b) 0.125 cm, and (c) 0.25 cm.

b.　Varying Hole Radius with a Q value of 50

For this set of simulations, the quality factor was $Q=50$, representing a loss of 1% of the energy due to absorption at each mirror surface. The hole radius was again varied from 0.05 cm to 0.40 cm. The range was selected to provide a direct comparison between the highly-reflecting mirror surface and the more realistic mirror surface.

Figure 9 plots the overall results of the simulations showing a trend towards smaller hole radii. A smaller hole radius is expected to be necessary, since now that some of the energy is absorbed by the mirror surfaces, the out-coupling hole should be smaller to compensate for the absorption. Due to limitations on the numerical grid, the optimal hole radius was unable to be found, which appears to be less than 0.05 cm for this case.


Extraction for a Partially Absorbant Surface with a Hole
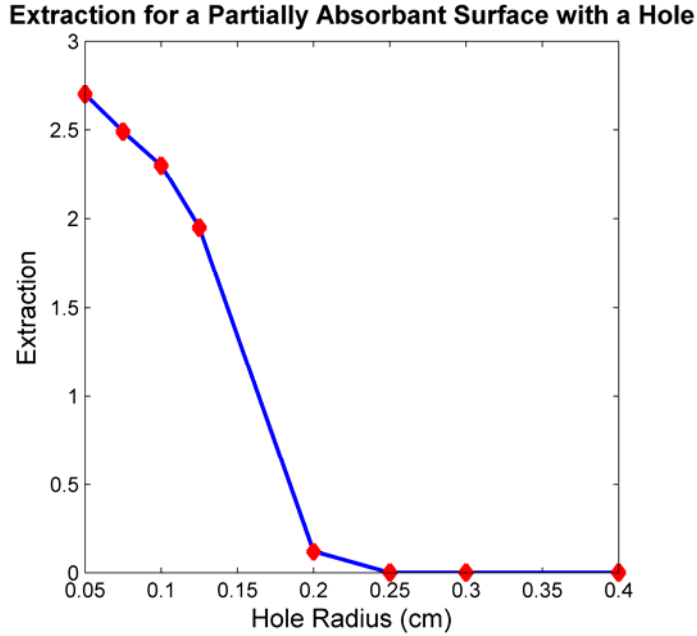
Figure 9.   Simulations results for 100pC bunch charge with Q=50

c.   *Varying the clipping gap for the theoretical simulations*

Since the longer wavelengths expand more rapidly than shorter wavelengths, absorbers were simulated at the ends of the undulator to clip a portion of the field that might scrape in the ends of the undulator. The gap between the absorbers was varied from 0.3 cm to 3.0 cm while the hole size was kept constant at 0.125 cm. For the results in the previous section, the absorbing gap was kept constant at 1.4 cm.

Figure 10 shows the results of the simulations, and finds that there is an optimal clipping gap of 1.5 cm for this set of parameters. As the gap size increases past the optimal there is little change in the extraction levels. This intuitively makes sense

21

because if the size of the gap keeps increasing, eventually there is no clipping. Past that threshold, there should be no change to the extraction since no energy is being lost to the absorbers.
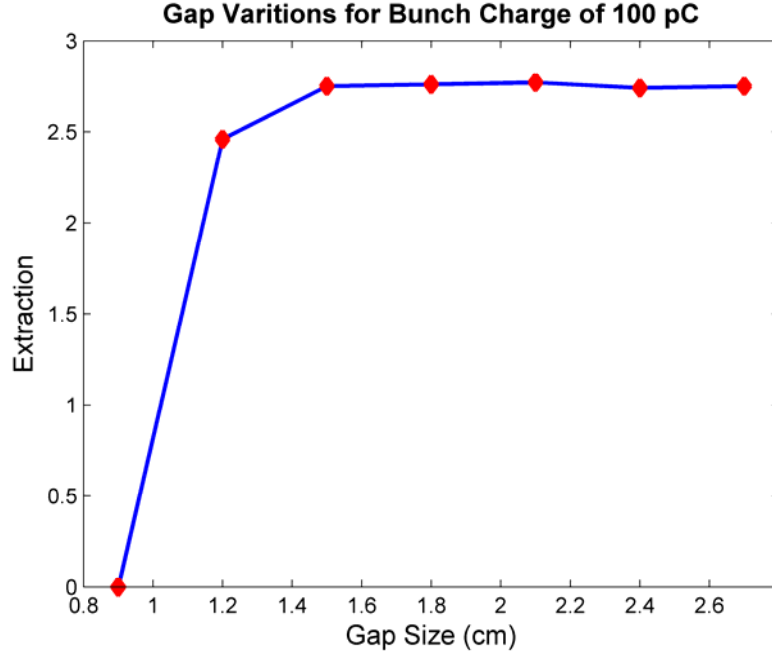
Figure 10.   Simulation results for Gap variations.

Figure 11 shows the simulation output for the optimal gap of 1.5 cm. It can be seen in that the mode shape is starting to become slightly less Gaussian in (a) and (c). This means that slightly more energy is going into higher-order modes, and shows that clipping can be used to force the optical mode into the fundamental.
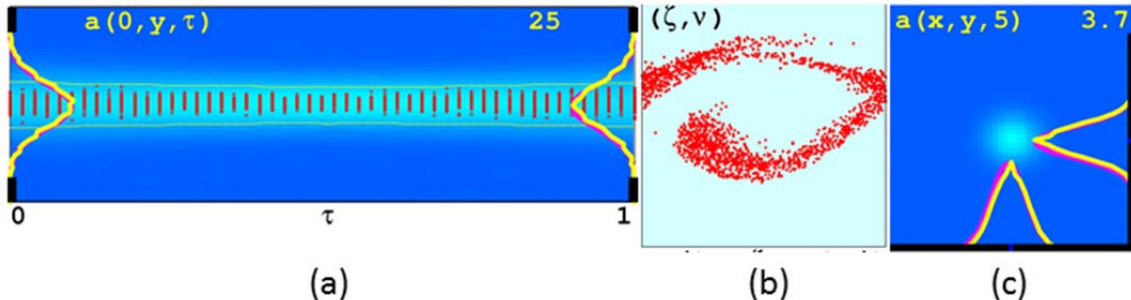

Figure 11.   Simulation output for gap of 1.5 cm.

2. 200 pC Bunch Charge Simulations

Simulations were also conducted for the 200 pC bunch charge, again varying the same parameters: the quality factor Q, the radius of the hole, and the clipping gap.

a. *Varying Hole Radius with a high Q value*

In the same way as with the 100 pC simulations, the set of simulations were conducted over a range of hole radii with $Q \sim 10^{10}$. The same hole radius range of 0.05 cm to 0.40 cm was utilized.

The results of the simulations are shown in Figure 12. The results show an optimal value for the hole radius of 0.15 cm with a corresponding extraction of 2.9%. The optimal hole size is slightly larger than the 100 pC case since there is more gain per pass with the 200 pC bunch, which allows more losses in steady-state.
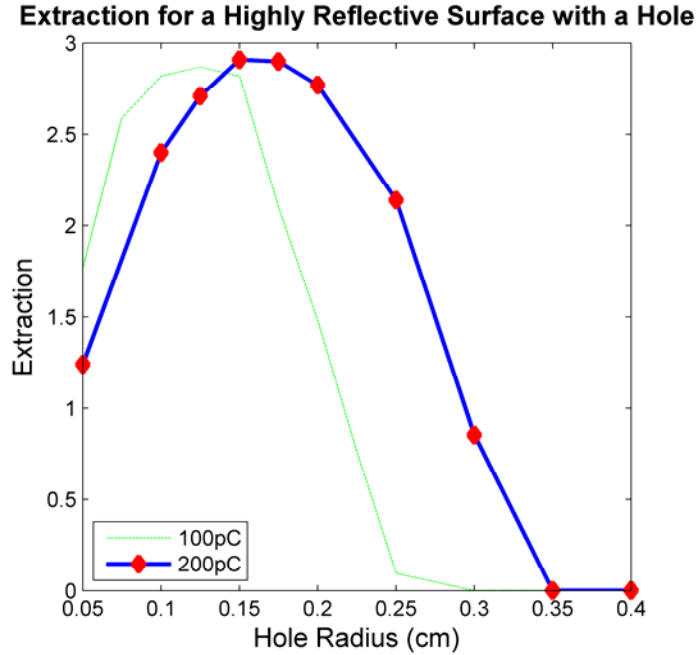

Figure 12. Simulations results for 200 pC bunch charge with $Q=10^{10}$

Figure 13 displays the output results for the optimal hole radius of 0.15 cm showing a well-bunched distribution in phase space in Figure 13 (b) and slight perturbations in the mode shape due to the hole in Figure 13 (c).
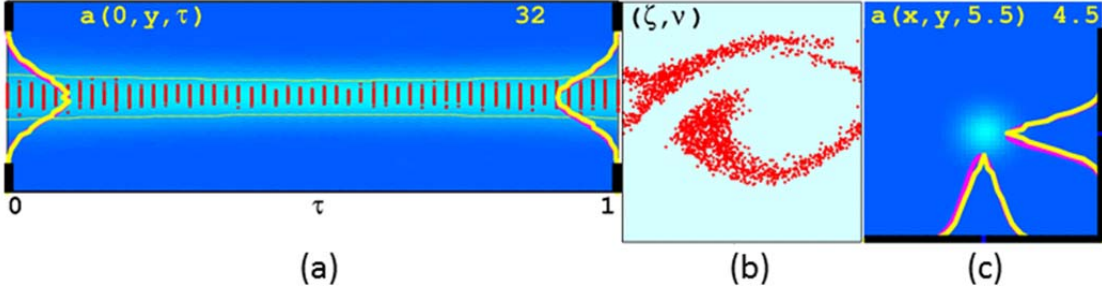
Figure 13.   Simulation output for hole radius of 0.15 cm.

b.   *Varying Hole Radius with a Q value of 50.*

For this set of simulations, the quality factor was $Q = 50$. As previously mentioned, this represented a loss due to absorption at the mirror surfaces. The hole radius range again was from 0.05 cm to 0.40 cm.

Figure 14 illustrates the overall results of this set of simulations directly compared to the 100 pC case. It shows that there was an increase in the optimal hole radius compare to the smaller value as seen in the previous case. For this set of simulations, the optimal hole radius is 0.10 cm and produced an extraction of 2.9%. The optimal hole radius is larger than the 100 pC case, since the higher gain per pass from the 200 pC bunch charge can tolerate more round-trip losses due to absorption and out-coupling.
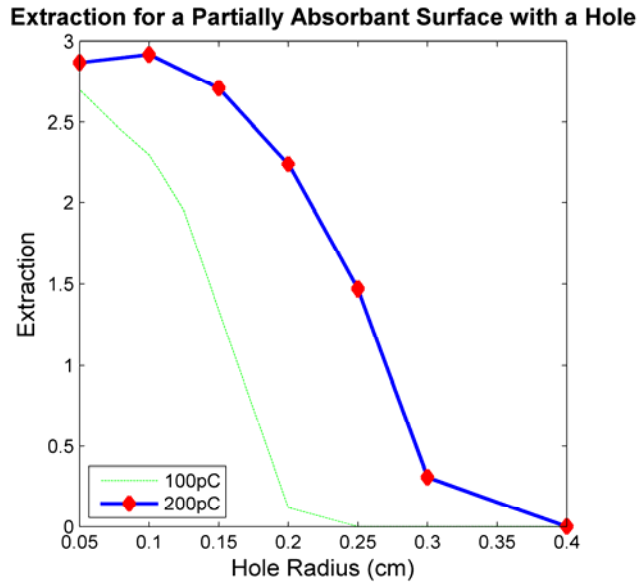
Figure 14.   Simulations results for 200 pC bunch charge with Q=50

Figure 15 shows the a comparison between the optimal hole radius of 0.05 cm for 100 pC case and the 200 pC optimal hole radius of 0.15 cm both with a $Q \sim 50$. Although the dimensionless amplitudes are not very different, the mode shape on the out-coupling mirror shows that this set of parameters will include higher-order modes as the hole size increases.
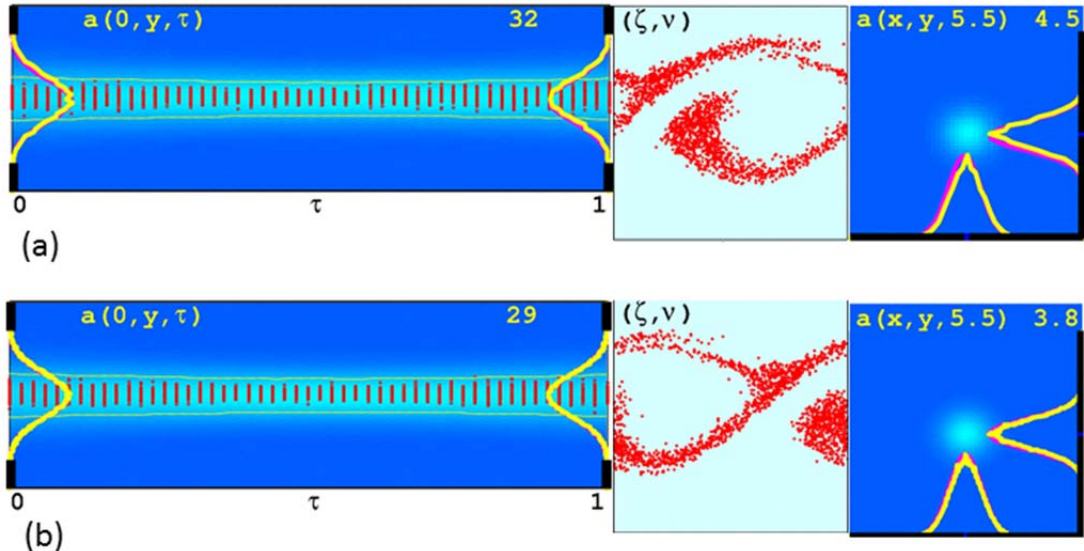
Figure 15.   Simulation output for hole radius of (a) 0.05 cm with 100 pC and (b) 0.15 cm with 200 pC.

c.   *Varying the clipping gap for the theoretical simulations*

Again, simulations were conducted varying the size of the absorbing gap over the range of 0.3 cm to 3.0cm.

Figure 16 shows the results of the simulations. The optimal gap in this case is 1.2 cm with an extraction of 3.0%. After the peak extraction was reached, the plot leveled off much like it did for the 100pC set.
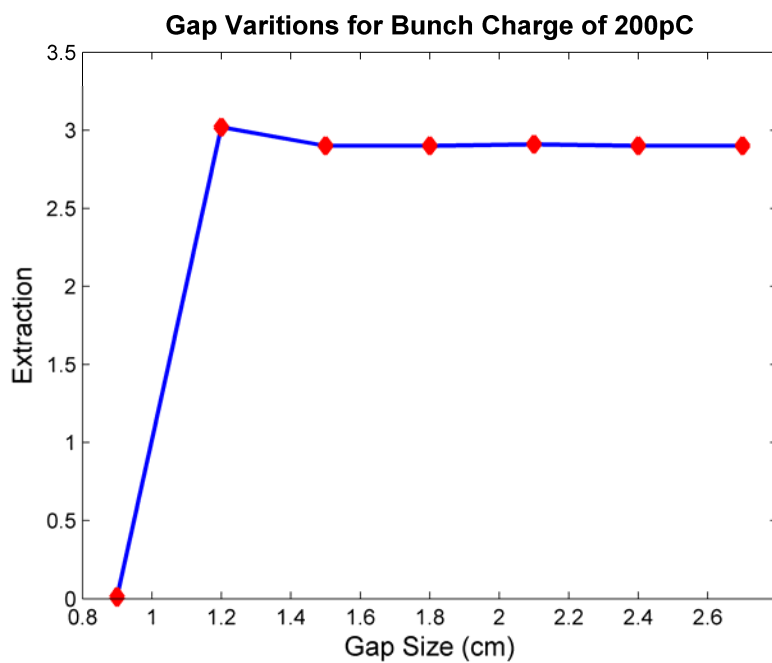
Figure 16.   Simulation results for Gap variations.

V. MESH OUT-COUPLING

Mesh out-coupling is another out-coupling technique that does not use a conventional partially transparent mirror. Instead, the light in this technique will out-couple through a metallic mesh. There are two types of meshes that can be considered for this application. The first type is the typical metallic mesh that uses thin strips of metal with no substrate and is referred to as an inductive mesh [11]. The second type uses a thin metallic pattern deposited on a substrate and is known as a capacitive mesh [11]. Both can have either circular or square symmetry and are illustrated in Figure 17. The mesh with square symmetry can be parameterized by three variables: the mesh period, g, the grid spacing, a, and the mesh thickness, t.

(a) inductive grid   (b) capacitive grid
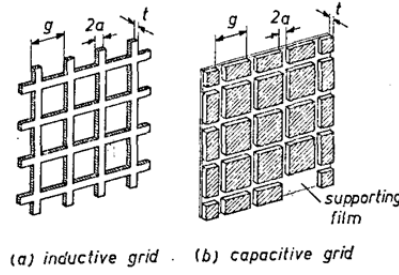
Figure 17.   Illustrations of freestanding (a) inductive metallic mesh and
(b) capacitive mesh with square symmetry.
From [11] t is the thickness of the mesh, g is the mesh period,
and a is the grid spacing.

Mesh out-coupling has been proven to work in the far infrared region of the spectrum [12]. While there are several ways to implement this technique [13], two will be discussed in this thesis: single mesh out-coupling and double mesh out-coupling. Both techniques will use an inductive mesh as the out-coupler in the thin mesh regime where $t \ll a$, with the assumption that there are no losses due to absorption in the mesh.

A.   OPTICAL PROPERTIES OF A SINGLE MESH

The optical properties of a single mesh can be derived and analyzed to show that a single mesh can be utilized as a reflective surface. Previous study of this interaction has provided results that were used in creating parameters for this thesis [12]. The analysis

from this study showed that a single mesh of square symmetry has optical properties that are independent of polarization because the mesh can be considered as the superposition of two crossed strip gratings if the ratio $a/g \leq 0.2$ is satisfied [12]. The same paper argued that if $g/\lambda < 1$, i.e. when the wavelength is longer than the mesh period, diffraction from the mesh edges is negligible [12].

Many of the coefficients needed to describe the optical properties of the mesh can be calculated based on an equivalent electric circuit that yields:

$$\Gamma = -\frac{Y/2}{1+Y/2} \qquad\qquad (V.1)$$

$$\tau_t = 1 + \Gamma \qquad\qquad (V.2)$$

where Γ is the complex amplitude reflection coefficient of the mesh, τ_t is the complex transmission coefficient of the mesh, $Y = -i(2/Z_0)(\lambda/g)$ is the admittance of the equivalent circuit, and $Z_0 = 2\ln(\csc(\pi a/g))$ is the impedance [12]. This assumes that there are no losses due to absorption in the mesh material.

The theoretical power reflectance is the magnitude of the complex amplitude reflection coefficient of the mesh squared, $R=|\Gamma|^2$. This can be used to show how the single mesh reacts to light that is normally incident onto it. In Figure 18, the power reflectance was plotted as a function of g/λ and parameterized over $0.04 \leq a/g \leq 0.20$. The figure shows that when λ is much larger than g, the single mesh tends to reflect most of the power. From this, it can be seen that the single mesh can be used in place of a mirror in the optical cavity of a long wavelength FEL, with the mesh parameters chosen to produce a desired quality factor for the cavity for a fixed wavelength.

Power Reflectance of a Single Mesh Out-Coupler
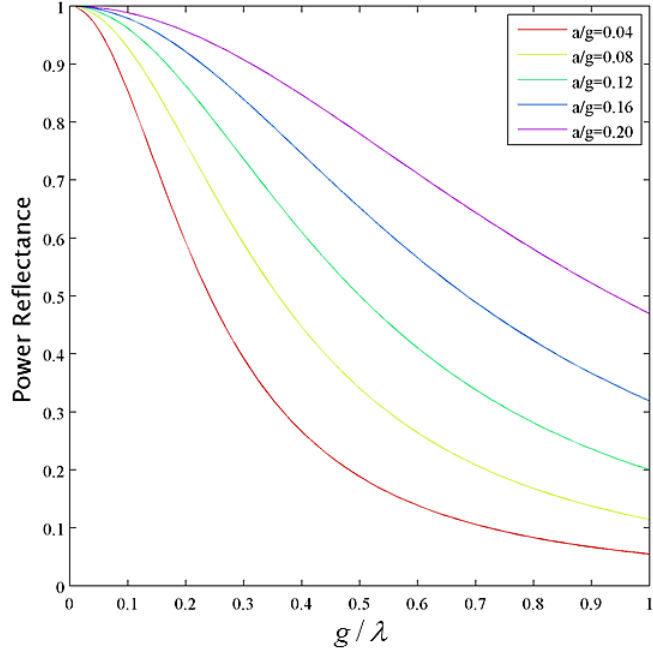
Figure 18.   Power reflectance of a single metallic mesh vs. g/λ where each curve is parameterized by a/g. After [12]

B.   DOUBLE MESH OUT-COUPLING

While a single mesh can be used as an out-coupler, a more flexible design uses a double mesh. Instead of using one freestanding metallic mesh, two freestanding metallic meshes are used in parallel and separated by some distance typically on the order of an optical wavelength, λ. Then, the total transmission and reflection from both meshes depends not only on the properties of each individual mesh, but also by the separation between them, much like a Fabry-Pérot Interferometer (which will be discussed in the following section of this chapter). Whereas the optical properties of the single mesh were strongly dependent on λ, the extra degree of freedom afforded by a double mesh allows one to maintain the constant set of optical properties across a range of wavelengths by adjusting the separation between the meshes [14].

1. Fabry-Pérot interferometer

A Fabry-Pérot interferometer (FPI) consists of two partially transparent, parallel mirrors separated by a medium or vacuum. The FPI is also used in a variety of applications including but not limited to optical resonators and spectrometers.

Figure 19 illustrates how a FPI transmits and reflects light, where s is the distance separating the two parallel reflecting surfaces, θ is the internal angle of incidence, and E_0 is the initial amplitude of the incident wave. As the wave travels through the FPI, each reflection creates a partial wave that is either transmitted or reflected. The subsequent internal reflections create, in principle, an infinite number of partial waves [15].
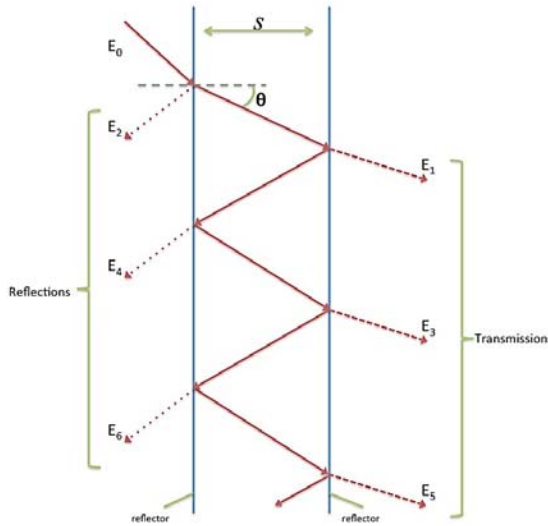
Figure 19.   Interaction between an incident light beam and a FPI.

Each partial wave acquires a phase shift per pass through the interferometer according to

$$\delta = \frac{4\pi n s \cos\theta}{\lambda} \tag{V.3}$$

where n is the index of refraction of the medium between the two surfaces, and λ is the wavelength of the incident wave, E_0, in vacuum. The partial waves that are reflected (E_2, E_4, E_6, …) are then calculated as

$$E_2 = rE_0 \; , \; E_4 = t^2 rE_0 e^{i\delta} \; , \; E_6 = t^2 r^3 E_0 e^{2i\delta} \; , \; \dots$$

30

where r and t are the amplitude reflection coefficient and the amplitude transmission coefficient respectively and are assumed to be equal for all reflections and transmissions. Similarly, the partial waves that are transmitted, (E_1, E_3, E_5, ...), are also calculated as

$$E_1 = t^2 E_0 , \ E_3 = t^2 r^2 E_0 e^{i\delta} , \ E_5 = t^2 r^4 E_0 e^{2i\delta} , \ ...$$

The sum of these waves constitute the amplitude of the transmitted wave and the reflected wave,

$$E_T = E_1 + E_3 + E_5 + ... + E_{2\sigma-1} \tag{V.4}$$

$$E_R = E_2 + E_4 + E_6 + ... + E_{2\sigma} \tag{V.5}$$

where E_T and E_R are the total transmitted amplitude and the total reflected amplitude, respectively, and σ approaches infinity. When the values of the partial waves are substituted into Equation V.4 and Equation V.5, they become

$$E_T = t^2 \left(1 + r^2 e^{i\delta} + r^4 e^{2i\delta} + ... \right) E_0 , \tag{V.6}$$

$$E_R = \left[r + t^2 r e^{i\delta} \left(1 + r^2 e^{i\delta} + r^4 e^{2i\delta} + ... \right) \right] E_0 . \tag{V.7}$$

It can now be seen that the total complex amplitudes both contain an infinite geometric series [15]. As such, the amplitudes can be rewritten as

$$E_T = \frac{T}{1 - Re^{i\delta}} E_0 , \tag{V.8}$$

$$E_R = \frac{\left(1 - e^{i\delta} \right) \sqrt{R}}{1 - Re^{i\delta}} E_0 , \tag{V.9}$$

where $R = r^2$ is the fraction of intensity reflected at each interface and $T = t^2$ is the fraction of intensity transmitted at each interface.

If the intensity of initial wave is defined as $I_0 = E_0^* E_0$, the ratio of transmitted intensity to the initial intensity can be described as

$$\frac{I_T}{I_0} = \frac{E_T^* E_T}{E_0^* E_0} = \frac{\left(1 - R^2 \right)}{\left(1 - R^2 \right) + 4R \sin^2 \left(\delta/2 \right)} . \tag{V.10}$$

31

Similarly, the ratio of reflected intensity to the initial intensity can be described as

$$\frac{I_R}{I_0} = \frac{E_R^* E_R}{E_0^* E_0} = \frac{4R\sin^2(\delta/2)}{\left(1-R^2\right)+4R\sin^2(\delta/2)} \qquad (V.11)$$

An assumption of Equations V.8 through V.11 is $r^2 + t^2 = 1$, i.e. there is no absorption occurring in the mesh material [15].

Figure 20 illustrates how the reflected energy depends on the phase shift for a given R. It can be seen that, even at large values of R, there are phase shifts where a large amount of the intensity is not reflected. From equation V.11, when $\delta = 2m\pi$, where m is an integer, the reflected intensity is equal to zero. As such, these phase shifts allow for complete transmission, assuming that there is no absorption.
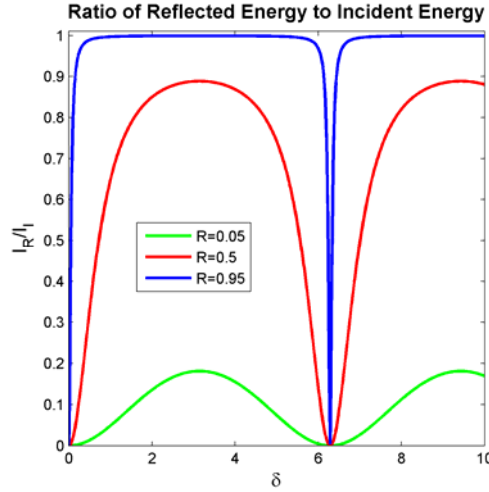

Figure 20.   Reflectance of a single metallic mesh. After [15]

Figure 21 displays the transmission ratio as a function of the phase shift. As seen, transmission maximums occur for the same phase value as reflection minimums.

**Ratio of Transmitted Energy to Incident Energy**
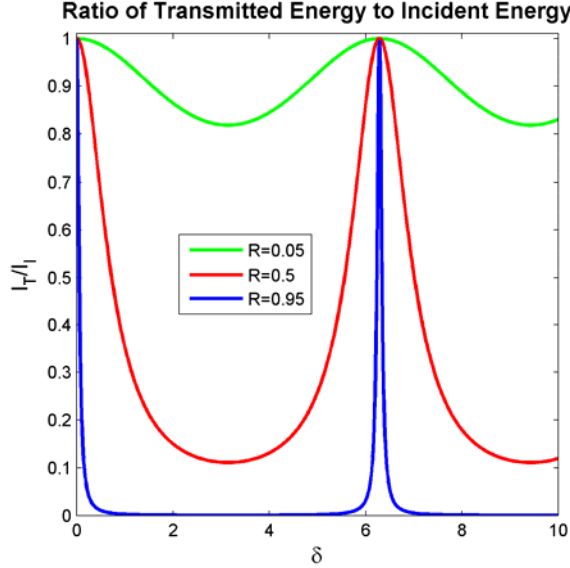
Figure 21.   Transmittance of a single metallic mesh. After [15]

When using two meshes to form an FPI, the only change to the FPI equations is the reflectance, R, is equated to the square of Γ from Equation V.1.

2.   Spherical Double Meshes

The NPS FEL 3D code assumes that the optical cavity is centered about the undulator and each mirror is assigned a radius of curvature based on the Rayleigh length of the cavity. This requirement motivated the consideration of spherical double meshes to ensure the feasibility of its use in the cavity [16].

Suppose a light beam has a normal incidence, $\theta = 0$, on the interferometer shown in Figure 19.   In that case, the path length the light would travel through the interferometer is 2s and is the same for any beam normally incident along the interferometer.   Therefore, all normally incident beams exit the interferometer with the same phase change. This ensures that the transmitted and reflected beams have the same phase.   If a set of spherical surfaces are considered for the interferometer, it must be proven that the path length traveled is approximately uniform for any normally incident beam at any point on the surface of the interferometer in order to preserve the uniform phase change of the reflected and transmitted beams.

33

Consider two identical spherical meshes that are separated by a distance s, as in Figure 22.
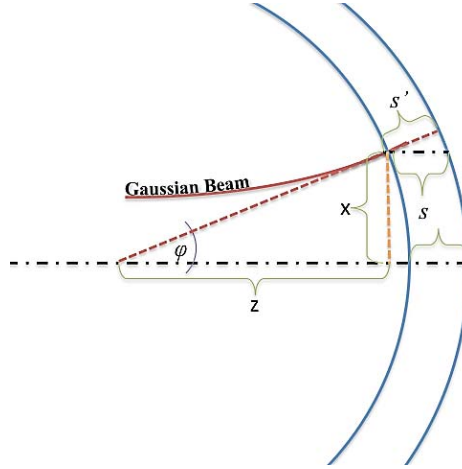

Figure 22.   Beam interaction with spherical double mesh. Illustration is not to scale as $z \sim$ meters, $x \sim$ centimeters, and $s \sim \lambda$.

It must be proven that there is no appreciable change in the phase of the beam as it travels through both meshes as a function of the divergence angle, φ; namely,

$$\Delta\delta = \delta(\varphi) - \delta(0) \ll 2\pi \qquad (V.12)$$

where $\Delta\delta$ is the change in the phase. From Equation V.3, it is shown that, $\delta(\varphi) = (4\pi s')/\lambda = (4\pi s)/(\lambda \cos\varphi)$ and $\delta(0) = 4\pi s/\lambda$. When substituted into Equation V.12, the result is

$$\Delta\delta = 4\pi/\lambda [s/\cos\varphi - s].$$

Figure 22 shows that $\varphi = \tan^{-1}(x/z) \approx \tan^{-1}(10^{-2}) \approx 10^{-2}$ rad. From this, the small angle approximation can be invoked, $\cos\varphi \approx \cos(10^{-2}) \approx 1$. Figure 22 also shows that $s \sim \lambda$. The result is that $\Delta\delta \ll 2\pi$.

3.   Equating Quality factor, Q, to Mesh Spacing

In order to simulate the out-coupling interaction of the double mesh out-coupler, the metal of the mesh was assumed to have negligible absorption for THz radiation. With this assumption, the only losses are transmission through the mesh. As such, the quality

factor, Q, that is defined to be inversely proportional to the loss of the cavity, is also inversely proportional to the energy transmitted through the double mesh, $Q \propto T^{-1}$. If the double mesh out-coupler is analyzed as an equivalent circuit with normalized admittances of each mesh being Y_1 and Y_2 [12], the power transmittance of the double mesh out-coupler can also be calculated in the following fashion:

$$T = |\tau_{DM}|^2,$$

where $\tau_{DM} = (\cos(ks) - iy_0 \sin(ks))(1 + \Gamma_I)$ is the complex amplitude transmission coefficient of the double mesh out-coupler [12], $k = 2\pi/\lambda$ is the wave number, s is the spacing between the meshes, $y_0 = (1 + Y_2 + i\tan(ks))/(1 + i(1 + Y_2)\tan(ks))$ is the admittance of the double mesh out-coupler, $\Gamma_I = (1 - y_I)/(1 + y_I)$ is the amplitude reflectance, and $y_I = y_0 + Y_1$ is the input admittance[12]. From the previously listed equations, it follows that a relationship between Q and s can be found, as shown in Figure 23 (a). The periodic nature of the relationship is the direct result of the periodic nature of the interference effects between the meshes, which can be seen in Figure 23 (b) where the reflectance, $R=1-T$, is plotted versus equivalent mesh spacing.
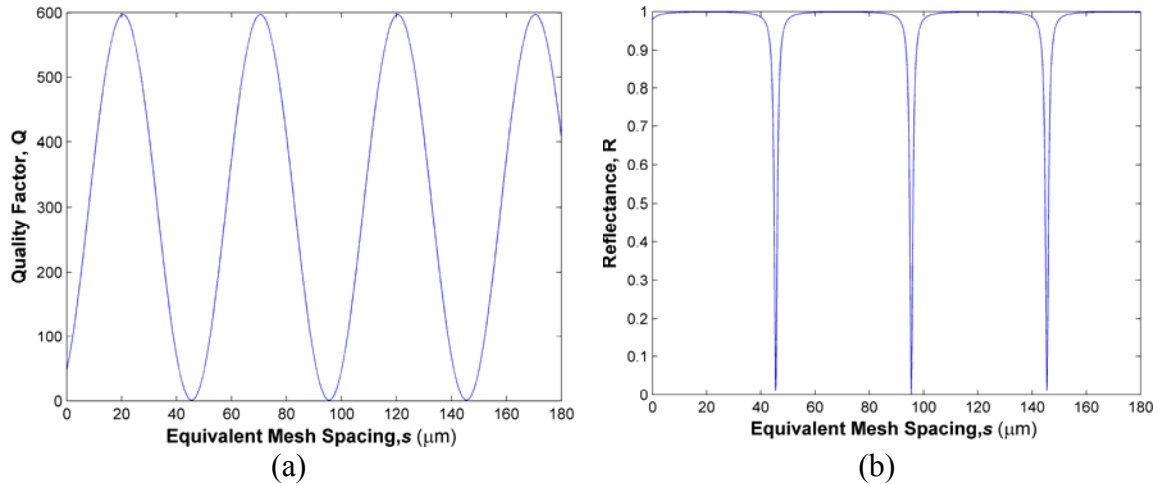

Figure 23.   (a) Quality factor as a function of mesh spacing.
(b) Reflectance as a function of mesh spacing.
Oscillations occur with a period of $n\lambda/2$.

The two plots in Figure 23 also specify a range of values for the mesh spacing. From graphical analysis, s is predicted to have a usable range of value between 96µm $\leq s \leq$ 103µm. Figure 23 (b) shows that if s is less than 96µm, the reflectance approaches zero and that would not allow net gain in the optical cavity. If s is greater than 103µm, the reflectance approaches unity at which point no light is being out-coupled from the cavity. Due to the cyclic nature of the interferometer, there are also other values of s that yield the same optical properties. In this thesis, only the values around 100μm will be considered.

The motivating factor for finding an equivalent mesh spacing for a given Q, flows from the prohibitive nature of creating a computational model of the mesh structure. The difficulties lie in that the model would need to be on the scale of centimeters with openings on the scale of microns. And each opening would need to have enough grid points over it to satisfactorily represent the results. This would require large amounts of computational time, on the order of weeks per simulation run. In the approximations used here, the macroscopic optical properties of the double mesh can be used with a degree of confidence in the results.

C. SIMULATION RESULTS

With the relationship between Q and s established, simulations were conducted using the NPS 3D oscillator FEL code and the parameters listed previously, and again categorized into two groups based on the electron bunch charge.

1. 100pC Bunch Charge Simulations

Simulations were conducted varying the quality factor over the range $5\leq Q \leq 100$ in the simulation code, to represent a corresponding mesh spacing, s, as discussed in a previous section. The mesh parameters used in the conversion of Q to s were a/g=0.16 and g/λ=0.20 which corresponded to a single mesh power reflectivity of 95%. These parameters satisfy the condition for long wavelengths.

Figure 24 shows that as the spacing is increased, the extraction increases to a peak and appears to begin to decrease. If the reflectance is too low, there is too little net gain in the cavity to exceed the losses. If the reflectance is too high, the fields inside the

cavity build up to such a large value that the electrons overbunch, reducing the extraction, as discussed in the previous chapter.. The extraction plot also shows that there is a peak extraction value of 2.88% when $R \approx 98\%$ which equates to $Q=75$, and an equivalent mesh spacing of $s \approx 101 \mu m$.
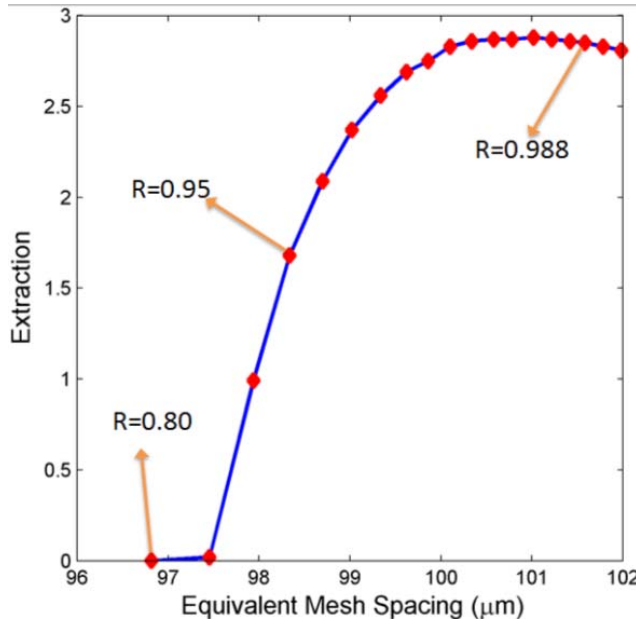

Figure 24.   The extraction from a double mesh out-coupler with bunch charge
of 100 pC. The Equivalent Mesh spacing directly corresponds
to the range of Q: 5≤Q≤95.

Figure 25 displays the output diagrams for the peak extraction. It should be noted that the mode is close to the fundamental Gaussian as seen in Figure 25 (b). This is preferable because the energy produced can then be focused into a smaller spot in an application.
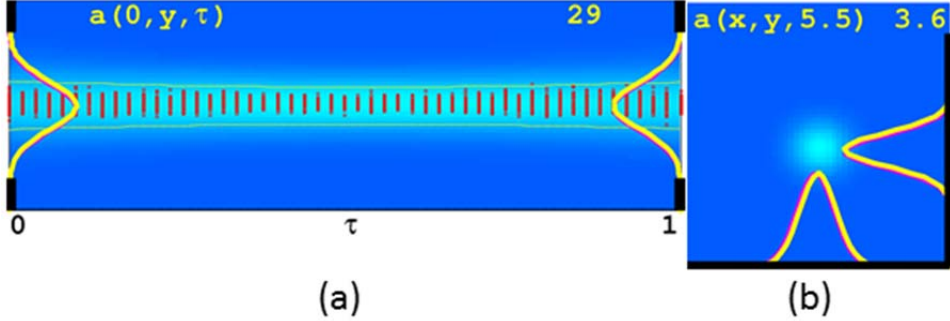
Figure 25.   (a) Simulation output of the evolution of the optical field
inside the undulator. (b) Optical mode shape
at the out-coupling mesh surface.

2.   200 pC Bunch Charge Simulations

Simulations were also conducted for a bunch charge of 200 pC by varying the quality factor over the range of Q values previously stated. Figure 26 illustrates how the simulated FEL performed with the increase in bunch charge. The plot shows that the peak extraction, 2.9% was approximately the same as the 100 pC case. The optimal reflectivity was $R=0.97$, which corresponds to a mesh spacing of $s \approx 99\,\mu m$ and $Q=35$. However, the simulated FEL did perform better over a broader range of mesh spacing. This can be attributed to the fact that the increase in the bunch charge directly correlates to an increase in net gain per pass.
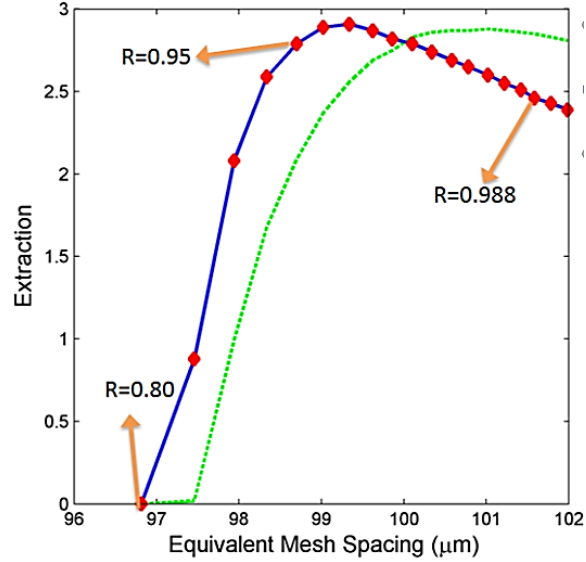
Figure 26.   The extraction from a double mesh out-coupler with bunch charge
of 200 pC. The green dotted line represents the results
from the 100 pC case. The Equivalent Mesh spacing directly
corresponds to the following range of Q: $5 \leq Q \leq 95$.

Figure 23 displays the output diagrams for the peak extraction. It should be noted that the mode shape in Figure 27 (b) is once again close to the fundamental Gaussian.
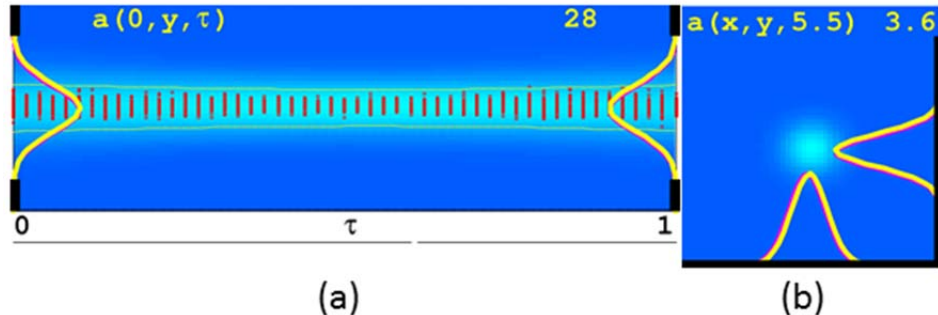

Figure 27.   (a) Simulation output of the evolution of the optical field inside the
undulator field amplitude in the optical cavity.
(b) Optical mode shape at the out-coupling mesh surface.

3.   Conclusion

The double mesh out-coupler simulations showed the FEL had extraction levels comparable to hole out-coupling and traditional partially transparent mirrors, as would be expected. Unlike hole out-couplers, mesh out-couplers will not disturb the transverse mode shape as long as $\lambda \gg g$. For larger values of mesh spacing, the 100 pC bunch charge may have a larger range of relatively high extraction, whereas the 200 pC bunch charge has better performance even at small spacing values.

VI.   FUTURE WORK

Several THz FEL out-coupling methods were studied in this thesis, including hole and double mesh out-coupling.   Another method uses zone plate diffractive optical elements. Zones plates are surfaces that use diffraction to focus incident light. As seen in Figure 28, the zone plate is comprised of concentric rings, or zones, that alternate between being transparent and opaque.   The transparent zones are spaced to promote constructive interference of the light at a specified focal point. To achieve this, the zone radii must be determined by $r_n = \sqrt{n\lambda f + \left(n^2 \lambda^2\right)\!/4}$, where n=1, 2, 3, ..., is the integer number of the zone, f is the distance to the focus point, and λ is the wavelength of light being focused [17].
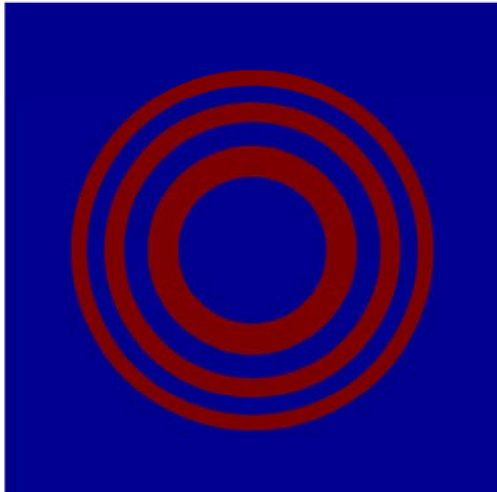

Figure 28.   Zone plate with 5 zones. Blue areas are opaque and
red areas are transparent.

Figure 29 shows the diffraction pattern in the plane of a zone plate at the focus resulting from five zones. Constructive interference produces a small, central peak at the focus, with a faint series of concentric rings due to higher diffraction orders.

41
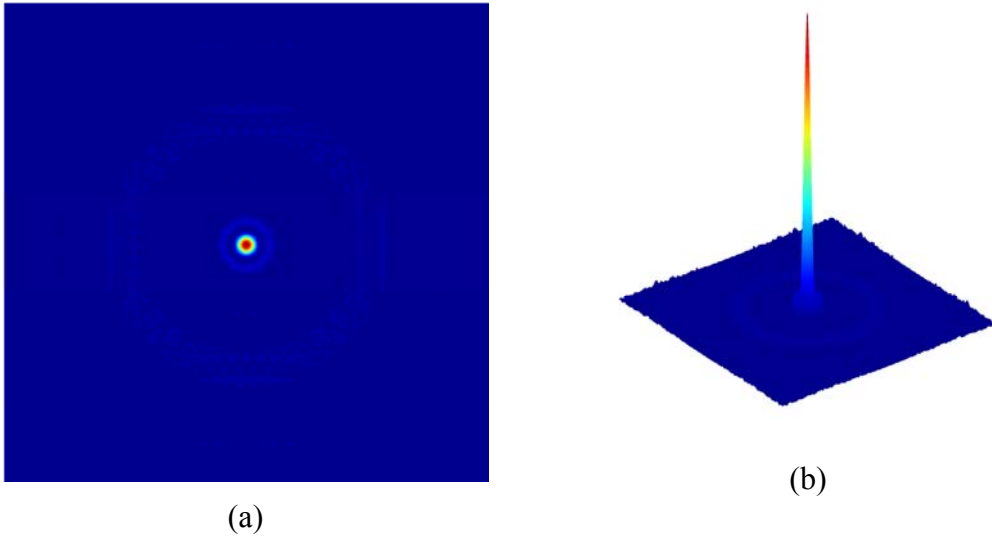
Figure 29.   (a) 2D output intensity of light out-coupled using a zone plate at focal point.
(b) 3D output intensity of light out-coupled through a zone plate

This unique method for out-coupling was previously considered to analyze whether it was possible to use a zone plate in a resonator [18]. The analysis showed that under certain conditions, namely, when the focal length is less than the resonator length, a zoned out-coupler would be feasible [18], [19].

The NPS 3D FEL code is currently being modified to simulate mirrors with zone structures. When this modification is complete, simulations should be conducted in order to examine the viability of this method for use in the THz regime.

VII. CONCLUSION

There are many current and potential applications of intense, coherent THz light sources, including basic physics experiments, military and homeland security applications. The FEL is already a powerful source of coherent light in many parts of the electromagnetic spectrum, including THz. From this motivation, this thesis explored multiple out-coupling techniques for an FEL operating $\sim 100\mu m$.

Through simulation using the NPS 3D FEL code, hole out-coupling was shown to be a viable method for out-coupling in the THz regime. It was seen that the hole had an effect on the optical mode in the cavity, and that there was an optimal hole size for maximum extraction. This optimal hole size was shown to be affected by changes in the bunch charge and the amount of absorption of the mirror material. The hole was also shown to affect the transverse mode shape of the beam; when the hole radius was increased, alterations in the mode shape increased.

As suggested from a previous study, beam clipping at the ends of the undulator was shown to improve mode quality when using hole out-coupling. An optimal amount of clipping was determined for the optimal hole radii studied in this thesis.

Double mesh out-coupling was also shown to be potentially a good method for THz out-coupling. The reflectance of the double mesh out-coupler was shown to increase as the spacing between the meshes increased. An optimal reflectance, corresponding to an optimal mesh spacing, was determined for different values of bunch charge. It was also shown that mesh out-coupling has very little effect on the optical mode shape. A double mesh has the additional advantage that it can be adjusted to perform well over a broad range of wavelengths, to take advantage of the FEL's inherent tunability.

THIS PAGE INTENTIONALLY LEFT BLANK

LIST OF REFERENCES

[1]   W. B. Colson. "Electric ship weapon systems," PH 4858 course notes. Naval Postgraduate School, Monterey, CA, Fall 2011.

[2]   N. M. Haegel. "Modern physics," PH 2652 course notes. Naval Postgraduate School, Monterey, CA, Winter 2010.

[3]   K. Cohn. "Free Electron Laser physics," PH 4055 course notes. Naval Postgraduate School, Monterey, CA, Winter 2010.

[4]   N. M. Haegel. "Physics of electromagnetic sensors and photonic devices," PC 3200 course notes. Naval Postgraduate School, Monterey, CA, Fall 2011.

[5]   M. W. Zemansky, *Heat and Thermodynamics* (5th ed.). New York, NY: McGraw-Hill, 1968.

[6]   D. Halliday, R. Resnick, and J. Walker, "Temperature, heat, and the first law of thermodynamics," in *Fundamentals of Physics* (8th ed.). New York, NY: Wiley & Sons, 2007, pp. 476.

[7]   A. Zimmer. "Terahertz Free-Electron Laser optical design and simulation." M.S. thesis, Naval Postgraduate School, Monterey, CA, 2010.

[8]   A. E. Siegman. "Wave optics and Gaussian beams" in *Lasers*. Sausalito, CA: University Science Books, 1986, pp. 626–662.

[9]   Wikipedia, the free Encyclopedia. (13 September 2006). "File:TEMmn.png"[online]. Available: http://en.wikipedia.org/wiki/File:TEMmn.png

[10]   C. O. Weiss, "Optically pumped FIR-Laser with variable Fabry-Perot output coupler*," Appl. Phys*., vol. 13, pp. 383, 1977.

[11]   R. Ulrich, "Far-infrared properties of metallic mesh and its complementary structure," *Infrared Physics*, vol. 7, pp. 37, 1967.

[12]   R. Ulrich, T. J. Bridges and M. A. Pollack, "Variable metal mesh coupler for Far Infrared Lasers," *Applied Optics*, vol. 9, pp. 2511, 1970.

[13]   M. R. Schubert, M. S. Durschlag, and T. A. DeTemple, "Diffraction limited CW optically pumped lasers," *IEEE J. Quantum Electron.*, vol. QE-13, pp. 455, June, 1977.

[14]   Professor K. Cohn (private communication), December 2011.

[15]   A. Yariv and P. Yeh, "Fabry-Perot Etalon," in *Photonics* (6th ed). New York, NY: Oxford University Press, 2007, pp. 160–164.

[16]   Professor K. Cohn (private communication), May 2012.

[17]   Wikipedia, the free Encyclopedia. (12 April 2012). "Zone Plate"[online]. Available: http://en.wikipedia.org/wiki/Zone_plate.

[18]   G. A. Emmons, "Analysis of a cylindrical laser resonator having a zoned output mirror," U.S. Army Missile Command, Redetone Arsenal, Alabama, Tech. Rep. RR-TR-70-22, September 1970.

[19]   C. D. Dennis, "Fresnel mirror in a Terahertz cavity," M.S. thesis, Naval Postgraduate School, Monterey, CA, 2012.

INITIAL DISTRIBUTION LIST

1.   Defense Technical Information Center
        Ft. Belvoir, Virginia

2.   Dudley Knox Library
        Naval Postgraduate School
        Monterey, California

3.   Chairman, Department of Physics
        Naval Postgraduate School
        Monterey, California

4.   Prof. William B. Colson
        Naval Postgraduate School
        Monterey, California

5.   Prof. Keith Cohn
        Naval Postgraduate School
        Monterey, California

6.   Prof. John B. Gilmer
        Wilkes University
        Wilkes-Barre, Pennsylvania